

VALIDATING RANGE-DEPENDENT, FULL-FIELD MODELS OF THE ACOUSTIC VECTOR FIELD IN SHALLOW WATER ENVIRONMENTS

KEVIN B. SMITH*

Department of Physics, Naval Postgraduate School, Monterey, CA 93943
kbsmith@nps.edu

Received 21 March 2007

Revised 27 July 2007

Numerical algorithms for computing acoustic particle velocity from a pressure propagation model are introduced. Implementation using both a parabolic equation and normal mode approach are considered. The parabolic equation model employed uses a split-step Fourier algorithm, although application of the technique is general to other parabolic equation models. Expressions for the normal mode equations are also presented, for both coupled and adiabatic mode models. Results for a Pekeris waveguide are presented for a point source, prompting a brief discussion of multipath influence on the estimation of the direction of energy flow. Approximate analytic solutions are used to validate the general results of both the models. Results for the range-dependent benchmark wedge are then presented, which show generally good agreement between the two types of models. The results from the two-way, coupled normal mode model provide potential benchmark solutions for the wedge and a means of confirming the accuracy of other models.

Keywords: Vector field; acoustic particle velocity; parabolic approximation; normal models.

Introduction

Interest in vector fields associated with the propagation of underwater acoustic energy developed in part from the theoretical work of Mann *et al.*¹ and experimental observations of D'Spain and colleagues.^{2,3} This was followed by signal processing studies reported by Nehorai,⁴ Hawkes and Nehorai,⁵ and Cray and Nuttall,⁶ among others. Although some modeling work has been previously reported,^{7,8} there has been a lack of rigorous developments in range-dependent, shallow water modeling of the acoustic vector field. While it may be considered a trivial matter, the introduction of some formal benchmarking measures would still be useful for the modeling community.

Little has been written about the behavior of the acoustic vector field in shallow water environments. Perhaps not surprising, the only thing that distinguishes the vertical plane behavior from the horizontal plane is the potential impact of multipath interference. But it is also in this additional effect that useful information may be extracted. Numerical

*Work completed while serving as Visiting Professor at the Naval Undersea Warfare Center, Newport, RI.

algorithms to compute such effects and rigorous tests of their accuracy are the goals of this paper.

The numerical algorithm employed to compute the acoustic vector field quantities from a parabolic equation model is described in Sec. 1. It is based on earlier work reported by Smith and Tappert⁷ and Smith *et al.*⁸ Section 2 develops the associated equations for use in normal mode models. A description of the implementation in a coupled mode model is also provided.

In Sec. 3, initial results are presented for a simple, range-independent Pekeris waveguide. The effects of multipath on estimates of the direction of flow are observed. In order to first ensure fine-scale accuracy, an analysis of the field in terms of a single mode is presented. This provides analytical solutions useful for confirming the behavior of the model. Expressions are also developed for more general, multi-mode propagation, which are employed to test both the PE and coupled mode model results for the range-independent scenario. Finally, the two-way coupled mode model is used to generate a set of accurate (potential benchmark) solutions and to confirm the accuracy of the PE method for the range-dependent benchmark wedge. Section 4 presents a summary of the analysis.

1. Parabolic Equation Modeling of Particle Velocity

We begin by stating the general form of the parabolic approximation to the Helmholtz wave equation for acoustic pressure,

$$\frac{\partial \psi}{\partial r} = -ik_0(1 - Q_{\text{op}})\psi = -ik_0 H_{\text{op}}\psi, \quad (1)$$

where ψ is the PE field function, defined by

$$p(\mathbf{r}) = P_0 \sqrt{\frac{R_0}{r}} \psi(\mathbf{r}) e^{ik_0 r}. \quad (2)$$

The 3D operator Q_{op} is defined by

$$Q_{\text{op}} = \sqrt{1 + \mu + \varepsilon + \nu}, \quad (3)$$

with $\mu = (1/k_0^2)(\partial^2/\partial z^2)$, $\nu = (1/k_0^2 r^2)(\partial^2/\partial \phi^2)$, and $\varepsilon = n'^2 - 1$, where n' is a generalized index of refraction term that accounts for the density fluctuations in the medium.

In this analysis, we shall focus on implementation using the split-step Fourier (SSF) technique.⁹ Specifically, the Monterey–Miami Parabolic Equation (MMPE) model¹⁰ has been upgraded to perform the calculations described here. This is purely for convenience, as the calculation of the velocity field will depend upon operations that are easily performed using Fourier transforms, and the MMPE model already utilizes such transforms extensively.

The SSF algorithm relies on an approximation of the form

$$1 - Q_{\text{op}} = H_{\text{op}} = T_{\text{op}} + U_{\text{op}} + V_{\text{op}}. \quad (4)$$

However, for the remainder of the work presented here, we shall assume that the uncoupled azimuth approximation is valid, and all motion is in the (r, z) plane. Then $\nu = 0$ and its

associated operator V_{op} also vanishes. The Thomson–Chapman wide angle PE (TC-WAPE) approximation for the SSF algorithm¹¹ is used here, i.e.

$$T_{\text{op}} = 1 - \left[1 + \frac{1}{k_0^2} \frac{\partial^2}{\partial z^2} \right] \quad (5)$$

and

$$U_{\text{op}} = -(n - 1) + U(\rho), \quad (6)$$

where $U(\rho)$ accounts for the density discontinuity at the water/bottom interface.¹⁰

By conservation of linear momentum, the acoustic particle velocity, $\mathbf{v} = (v_r, v_z, v_\phi)$, is related to the acoustic pressure by

$$\mathbf{v} = -\frac{i}{\omega\rho} \nabla p, \quad (7)$$

given that both \mathbf{v} and p have the same $e^{-i\omega t}$ time dependence. In cylindrical coordinates (neglecting azimuth), this becomes

$$\mathbf{v} = -\frac{i}{\omega\rho} \left[\frac{\partial p}{\partial r} \hat{r} + \frac{\partial p}{\partial z} \hat{z} \right]. \quad (8)$$

Separating the components, we find that the radial term may be expressed as

$$\begin{aligned} v_r &= -\frac{i}{\omega\rho} P_0 R_0^{1/2} \left[-\frac{\psi}{2r^{3/2}} + \frac{ik_0}{r^{1/2}} \psi + \frac{1}{r^{1/2}} \frac{\partial \psi}{\partial r} \right] \\ &\approx \frac{P_0}{c_0\rho} \sqrt{\frac{R_0}{r}} e^{ik_0 r} (1 - H_{\text{op}}) \psi \\ &= \frac{P_0}{c_0\rho} \sqrt{\frac{R_0}{r}} e^{ik_0 r} Q_{\text{op}} \psi, \quad r \gg \frac{1}{k_0}. \end{aligned} \quad (9)$$

This defines the general expression for computing the radial component of the particle velocity from any PE model based on Eq. (1). For the SSF algorithm, we apply Eqs. (4)–(6) to obtain

$$v_r(r, z) = \frac{P_0}{c_0\rho} \sqrt{\frac{R_0}{r}} e^{ik_0 r} [n - U_{\text{op}}(\rho) - T_{\text{op}}] \psi(r, z). \quad (10)$$

In the vertical plane,

$$v_z = -\frac{iP_0}{\omega\rho} \sqrt{\frac{R_0}{r}} e^{ik_0 r} \frac{\partial \psi}{\partial z}, \quad (11)$$

which can be solved using the FFT technique, i.e.

$$v_z(r, z) = \frac{P_0}{c_0\rho} \sqrt{\frac{R_0}{r}} e^{ik_0 r} FFT \left[i \frac{k_z}{k_0} IFFT(\psi(r, z)) \right]. \quad (12)$$

2. Normal Mode Modeling of Particle Velocity

We now consider an approach to modeling the velocity field in the context of coupled, normal modes. Following the notation of Jensen *et al.*,¹² the far-field pressure field in some j th range segment between r_j and r_{j+1} is given by the fully-coupled (two-way) normal mode expansion

$$p^{(j)}(r, z) = P_0 \sum_{m=1}^M [a_m^{(j)} H1_m^{(j)}(r) + b_m^{(j)} H2_m^{(j)}(r)] \Psi_m^{(j)}(z), \quad (13)$$

where $\Psi_m^{(j)}(z)$ are the depth-separated, normal modes within the j th range segment, the factors $a_m^{(j)}$ and $b_m^{(j)}$ define the amplitudes of the forward and backward propagating parts of the field, respectively, and

$$H1_m^{(j)}(r) = \sqrt{\frac{r_{j-1}}{r}} e^{iK_m^{(j)}(r-r_{j-1})}, \quad H2_m^{(j)}(r) = \sqrt{\frac{r_{j-1}}{r}} e^{-iK_m^{(j)}(r-r_{j-1})}. \quad (14)$$

At the interface between segment j and $j+1$, coupling coefficients are derived based on the continuity of pressure and radial displacement (or radial velocity). The former produces coupling coefficients defined by¹²

$$\tilde{c}_{nm}^{(j)} = \int \frac{\Psi_n^{(j+1)}(z) \Psi_m^{(j)}(z)}{\rho^{(j+1)}(z)} dz, \quad (15)$$

while the latter gives

$$\hat{c}_{nm}^{(j)} = \frac{K_m^{(j)}}{K_n^{(j+1)}} \int \frac{\Psi_n^{(j+1)}(z) \Psi_m^{(j)}(z)}{\rho^{(j)}(z)} dz. \quad (16)$$

As in the approach using PE, we seek expressions for evaluating the velocity field locally based on solutions of the pressure field. For the fully-coupled description just defined, the velocity field components are given simply by

$$v_r^{(j)}(r, z) = -\frac{i}{k^{(j)}(r, z)} \frac{P_0}{\rho^{(j)} c^{(j)}(r, z)} \sum_{m=1}^M K_m^{(j)} [a_m^{(j)} H1_m^{(j)}(r) - b_m^{(j)} H2_m^{(j)}(r)] \Psi_m^{(j)}(z) \quad (17)$$

for $r \gg 1/K_m^{(j)}$, where $c^{(j)}(r, z)$ is the local sound speed and $k^{(j)}(r, z)$ is the associated wavenumber, and

$$v_z^{(j)}(r, z) = -\frac{i}{k^{(j)}(r, z)} \frac{P_0}{\rho^{(j)} c^{(j)}(r, z)} \sum_{m=1}^M [a_m^{(j)} H1_m^{(j)}(r) + b_m^{(j)} H2_m^{(j)}(r)] \frac{d\Psi_m^{(j)}}{dz}(z). \quad (18)$$

Thus, the only additional computation beyond the existing solutions for the normal modes and their associated wavenumbers is the vertical derivative of the modes. Note that the modes, their derivatives, and modal wavenumbers may all be complex, in general, to account for volume losses and the evanescent spectrum.

Because the coupling coefficient defined in Eq. (16) was derived by assuming continuity of the radial velocity field, the solution to Eq. (17) must be smoothly continuous across range segment boundaries. Furthermore, the requirement of continuity of pressure across the range segment boundaries implicit in the coupling coefficients defined in Eq. (15) applies along the entire depth of the calculation. Thus, continuity of the vertical velocity field is also ensured. This justifies the use of the local expressions in Eqs. (17) and (18) without the need for special considerations in range-dependent environments. Evaluation of these expressions may then be expected to provide benchmark quality results in environments that require the full, two-way coupled solution.

More efficient, range-dependent solutions are obtained by making some one-way approximations. Readers are referred to Ref. 12 for details. By neglecting backscatter, one can simplify the forward coupling to a “single-scatter” approximation, whereby $a_m^{(j+1)}$ depends solely upon $a_m^{(j)}$ through the forward coupling coefficients. Likewise, we neglect the backward propagating solutions in the calculations of the velocity field such that Eqs. (17) and (18) reduce to

$$v_r^{(j)}(r, z) = -\frac{i}{k^{(j)}(r, z)} \frac{P_0}{\rho^{(j)} c^{(j)}(r, z)} \sum_{m=1}^M K_m^{(j)} a_m^{(j)} H_1^{(j)}(r) \Psi_m^{(j)}(z), \quad (19)$$

for $r \gg 1/K_m^{(j)}$, and

$$v_z^{(j)}(r, z) = -\frac{i}{k^{(j)}(r, z)} \frac{P_0}{\rho^{(j)} c^{(j)}(r, z)} \sum_{m=1}^M a_m^{(j)} H_1^{(j)}(r) \frac{d\Psi_m^{(j)}}{dz}(z), \quad (20)$$

respectively.

For completeness, let us also consider a description of the field in terms of adiabatic normal modes. The pressure field can then be defined as¹²

$$p(r, z) \simeq \frac{iP_0}{\rho} \sqrt{\frac{2\pi}{r}} e^{-i\frac{\pi}{4}} \sum_{m=1}^M \Psi_m(z_s) \Psi_m(z) \frac{e^{i \int_0^r K_m(r') dr'}}{\sqrt{K_m(r)}}. \quad (21)$$

The description of the velocity field now easily satisfies

$$v_r(r, z) \simeq \frac{iP_0}{k(r, z) \rho^2 c(r, z)} \sqrt{\frac{2\pi}{r}} e^{-i\frac{\pi}{4}} \sum_{m=1}^M \sqrt{K_m(r)} \Psi_m(z_s) \Psi_m(z) e^{i \int_0^r K_m(r') dr'}, \quad (22)$$

and

$$v_z(r, z) \simeq \frac{P_0}{k(r, z) \rho^2 c(r, z)} \sqrt{\frac{2\pi}{r}} e^{-i\frac{\pi}{4}} \sum_{m=1}^M \Psi_m(z_s) \frac{d\Psi_m}{dz}(z) \frac{e^{i \int_0^r K_m(r') dr'}}{\sqrt{K_m(r)}}. \quad (23)$$

Again, the only additional calculation needed is a description of the vertical derivative of the modes.

The expressions given in Eqs. (17)–(20) have been incorporated into a version of the Couple97 model.^{12,13} It is worth noting that the incorporation of the vertical component, based on the derivatives of the mode shapes, was reasonably straightforward due to the use of the Galerkin matrix method. Since this method employs sinusoids as a basis set, the calculation of derivatives was trivial. This updated version of Couple97 can then be used to develop accurate solutions, in general, range-dependent environments. Specifically, we shall consider solutions to the ASA benchmark wedge.¹⁴

3. Validating Particle Velocity Field Calculations

To begin testing the PE implementation of the velocity field, we consider here a simple Pekeris waveguide of depth $D = 200$ m with a water column sound speed of $c_0 = c = 1500$ m/s, water density of $\rho = 1.0$ g/cc, bottom sound speed of $c_b = 1700$ m/s, bottom density of $\rho_b = 1.5$ g/cc, and no bottom attenuation. The source is in the middle of the water column at 100 m, transmitting a CW signal of 200 Hz. The typical, pressure transmission loss (TL) field, $20 \log_{10}(|p|/|P_0|)$ dB re R_0 , is provided in Fig. 1(a).

Employing the relationships above produces additional output in the form of complex particle velocity components (horizontal and vertical). Figures 1(b) and 1(c) show the structure of the fields of horizontal and vertical velocity components, respectively. Analogous to pressure transmission loss, we define the dB quantity $20 \log_{10}(|v_{r,z}|/|V_0|)$ dB re R_0 , where $V_0 = P_0/(\rho c_0)$. Close examination reveals some features that would be expected. First, the vertical component of velocity is very small (effectively zero) for short ranges near the source depth. This is consistent with a spherical wavefront emanating from a point source, which, along the depth of the source, will only have a radial component of velocity. Second, in all areas, the horizontal component is typically an order of magnitude larger than the vertical, consistent with the primarily radial direction of motion.

It is perhaps worth noting that in cases with multipath interference, the simple concept of relating wavefront propagation angles to local ratios of velocity components does not necessarily apply. In Fig. 2, the angle defined by $\theta = \tan^{-1}(\text{Re}(v_z)/\text{Re}(v_r))$ is displayed. Although critical angle stripping of high angle propagation removes wavefront energy at angles steeper than about 28° , the data shows local values up to nearly $\pm 90^\circ$ at all ranges and extending over all depths.

Before expanding our analysis to this multi-mode case, and to explain the physical justification for this local behavior, we shall first simplify the problem further. Let us assume that a single mode M is excited in a range-independent environment. Then

$$p(r, z) = \frac{iP_0}{\rho_0} \sqrt{\frac{2\pi}{r}} e^{-i\frac{\pi}{4}} \Psi_M(z_s) \Psi_M(z) \frac{e^{iK_M r}}{\sqrt{K_M}}. \quad (24)$$

The mode shape and corresponding horizontal wavenumber component were computed using a simple normal mode algorithm. The shape was then input into the MMPE model as a source starter. The horizontal wavenumber component for this mode is $K_5 \simeq 0.8342 \text{ m}^{-1}$, which corresponds to wavefront angles of propagation of $\theta_5 \simeq \pm 5.30^\circ$.

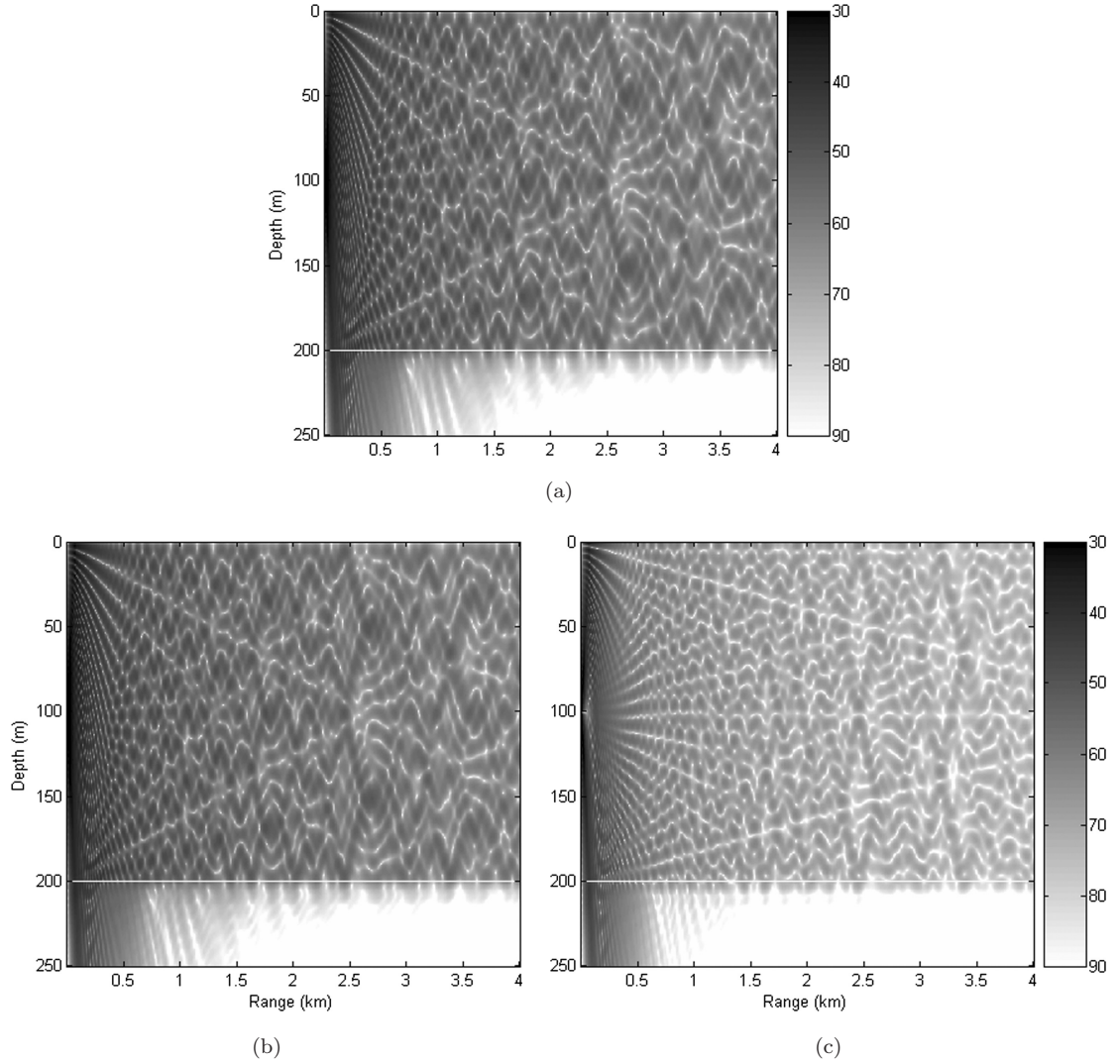


Fig. 1. Transmission loss plots at 200 Hz in Pekeris waveguide for point source at 100 m depth: (a) pressure; (b) radial component of particle velocity; (c) vertical component of particle velocity.

The associated particle velocity field is now defined by

$$v_r(r, z) = \frac{iP_0}{k\rho^2c} \sqrt{\frac{2\pi}{r}} e^{-i\frac{\pi}{4}} \sqrt{K_M} \Psi_M(z_s) \Psi_M(z) e^{iK_M r} \quad \text{for } r \gg \frac{1}{K_M}, \quad (25)$$

and

$$v_z(r, z) = \frac{P_0}{k\rho^2c} \sqrt{\frac{2\pi}{r}} e^{-i\frac{\pi}{4}} \Psi_M(z_s) \frac{\partial \Psi_M(z)}{\partial z} \frac{e^{iK_M r}}{\sqrt{K_M}}. \quad (26)$$

We see here that the ratio $v_z/v_r = (1/iK_M)/[(\partial \Psi_M/\partial z)/\Psi_M]$ is independent of r but has depth dependence.

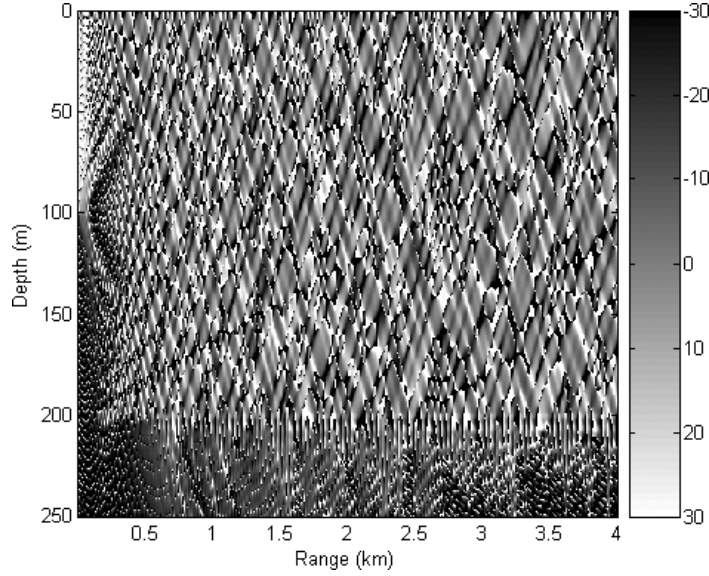


Fig. 2. Inverse tangent of ratio of real part of vertical component to real part of horizontal component of particle velocities.

Let us now take advantage of the fact that we have a simple, isospeed waveguide with mode shapes that satisfy a sinusoidal form in the water column, i.e.

$$\Psi_M(z) \propto \sin(\gamma_M z), \quad z < z_b, \quad (27)$$

where $\gamma_M = \sqrt{k^2 - K_M^2}$ is the vertical component of the wavenumber, and is a constant in this case. The horizontal and vertical wavenumber components are $K_M = k \cos \theta_M$ and $\gamma_M = k \sin \theta_M$, respectively, where θ_M is the angle of propagation of the wavefronts corresponding to this mode. This mode is formed by the interference of wavefronts propagating down the waveguide at angles $\pm \theta_M$. Thus, one might expect that the acoustic particle velocity field would clearly indicate this by producing v_z/v_r ratios consistent with this.

Examination of the pressure and velocity fields shows the expected banded structure of a mode 5 solution. Both the pressure and the horizontal components of particle velocity have nulls at the surface and bottom, while the vertical component has maxima at these depths. And as before, the horizontal component magnitude is roughly an order of magnitude larger than the vertical, also as expected. In Fig. 3, we display the inverse tangent of the ratio of the real part of the vertical component to the real part of the horizontal component. Again, this produces a range of propagation angle values, not the single-valued mode angle $\pm \theta_5$.

The vertical derivative of the mode is

$$\frac{\partial \Psi_M}{\partial z} \propto \gamma_M \cos(\gamma_M z). \quad (28)$$

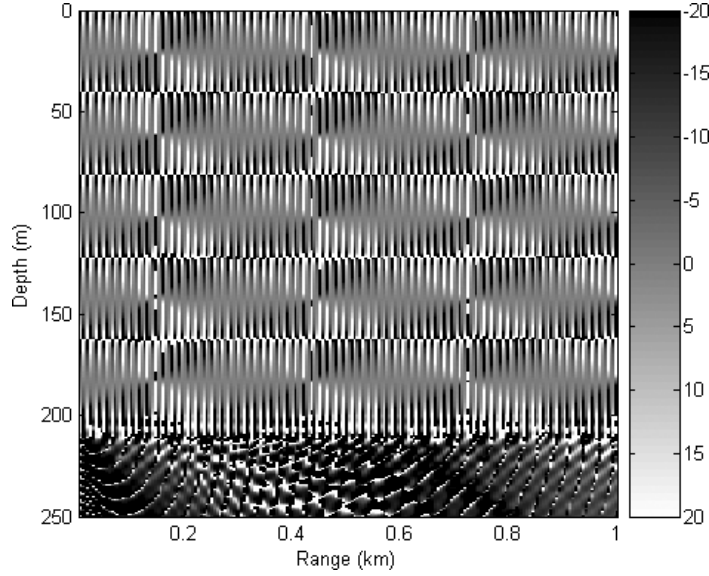


Fig. 3. Ratio of real part of vertical component to real part of horizontal component of particle velocities for mode 5. Note expanded gray scale to emphasize values away from mode propagation angle. Image sampling in range is insufficient to display full interference pattern.

The particle velocity component ratio then becomes

$$\frac{v_z}{v_r} = \frac{\gamma_M}{iK_M} \frac{\cos(\gamma_M z)}{\sin(\gamma_M z)} = -i \frac{\tan \theta_M}{\tan(\gamma_M z)}. \quad (29)$$

Equation (29) shows explicitly how the vertical and horizontal components of the velocity field are out of phase by 90° , and that this ratio is not constant. This indicates that the associated fluid motion is elliptical, in general. Although independent of range, it varies with depth in a periodic but noncontinuous way (not continuous through mode nodes).

In order to confirm that the model is generating appropriate solutions, some analytic functions are desired which can be used for validation. For comparisons with numerical results, we shall examine the following ratios:

$$\frac{\text{Re}(v_z)}{\text{Im}(v_r)} = \frac{1}{K_M} \frac{\frac{\partial \Psi_M}{\partial z}}{\Psi_M} = \frac{\tan \theta_M}{\tan(\gamma_M z)} \quad (30)$$

and

$$\frac{\text{Re}(v_z)}{\text{Re}(v_r)} = -\frac{\tan \theta_M}{\tan(\gamma_M z)} \cot\left(K_M r - \frac{\pi}{4}\right). \quad (31)$$

In Fig. 4(a), the ratio defined in Eq. (30) is utilized at an arbitrary range (0.5 km, in this case). Figure 4(b) displays the ratio defined in Eq. (31) at an arbitrary depth (90 m here). The results are presented over 1 km only in order to resolve the interference structure of wavelength scales. Although the range resolution barely resolves the interference scale, the results agree remarkably well with the analytical predictions. This suggests that the

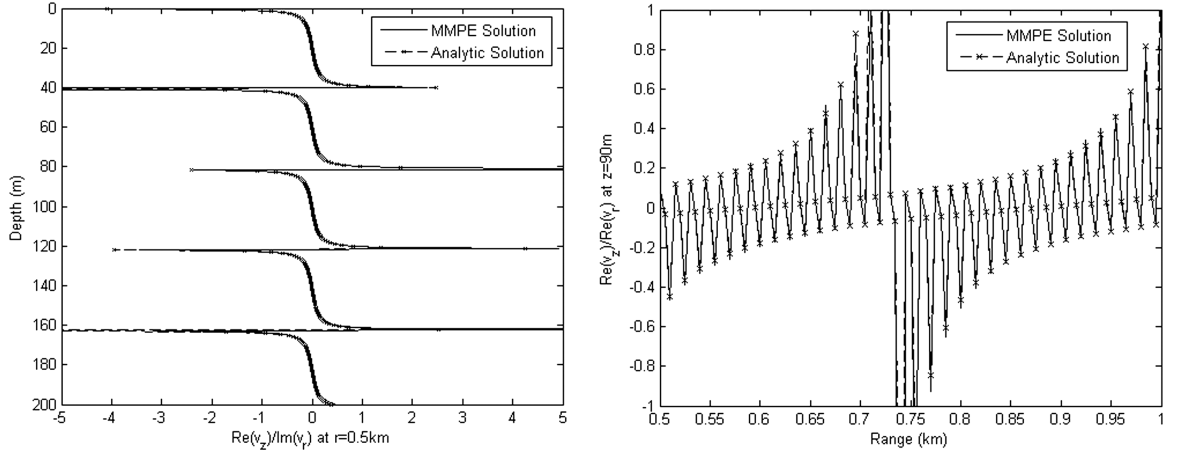


Fig. 4. Comparison of ratios defined by Eq. (30) at a range of 0.5 km (left) and Eq. (31) at a depth of 90 m (right) for single mode 5 calculation: MMPE (solid) and analytical solution (dash).

numerical algorithm for computing acoustic particle velocity from the PE code is working properly.

In order to compare with a more general but still analytically tractable case, we now consider the solution for many excited modes in the same range-independent Pekeris waveguide. We shall also include bottom attenuation of $\alpha = 0.5 \text{ dB}/\lambda$. While this is not an exceptionally challenging problem for models designed to handle range-dependence, there will be sufficient complexity in what follows to allow testing of the particle velocity calculations. Note that, in order to simplify the analytical description, we shall assume that the attenuation introduces a small perturbation to the wavenumber, i.e. $\delta_m \ll K_m$. Only the lowest order correction, the modal attenuation in range, will then be included. The mode shapes and computed wavenumbers will still be treated as real-valued. Thus, this solution does not provide a benchmark data set, but does provide a general check on the model's performance.

The point source solution in the Pekeris waveguide, including only M trapped modes and the lowest order correction for modal attenuation, is given by

$$p(r, z) = \frac{iP_0}{\rho} \sqrt{\frac{2\pi}{r}} e^{-i\frac{\pi}{4}} \sum_{m=1}^M A_m^2 \sin(\gamma_m z_s) \sin(\gamma_m z) \frac{e^{iK_m r}}{\sqrt{K_m}} e^{-\delta_m r}, \quad (32)$$

where $\gamma_m = \sqrt{(\omega/c)^2 - K_m^2}$ is the (positive) vertical wavenumber component for each mode $m < M$. Defining the normalization amplitude for these trapped modes in a Pekeris waveguide as $\int_0^\infty [\Psi_m^2(z)/\rho(z)] dz = 1$, we find

$$A_m^2 = \left[\frac{1}{2\rho} D - \frac{1}{4\rho\gamma_m} \sin(2\gamma_m D) + \frac{\sin^2(\gamma_m D)}{2\rho_b g_m} \right]^{-1}, \quad (33)$$

where D is the waveguide depth and $g_m = \sqrt{K_m^2 - (\omega/c_b)^2}$. Employing the perturbation expression $\delta_m = \omega/K_m \int_0^\infty [\alpha_e(z)/c(z)] \Psi_m^2(z) dz$ for the modal attenuation, we obtain

$$\delta_m = \frac{\omega}{K_m} \frac{\alpha_e}{c_b} \frac{A_m^2 \sin^2(\gamma_m D)}{2g_m}, \quad (34)$$

where $\alpha_e(\text{m}^{-1}) = \alpha(\text{dB}/\lambda) \times \lambda(\text{m})/8.686$ is the exponential attenuation of the bottom in units of m^{-1} . It follows then that

$$v_r(r, z) = \frac{iP_0}{k\rho^2 c} \sqrt{\frac{2\pi}{r}} e^{-i\frac{\pi}{4}} \sum_{m=1}^M \sqrt{K_m} A_m^2 \sin(\gamma_m z_s) \sin(\gamma_m z) e^{iK_m r} e^{-\delta_m r} \quad (35)$$

and

$$v_z(r, z) = \frac{P_0}{k\rho^2 c} \sqrt{\frac{2\pi}{r}} e^{-i\frac{\pi}{4}} \sum_{m=1}^M \gamma_m A_m^2 \sin(\gamma_m z_s) \cos(\gamma_m z) \frac{e^{iK_m r}}{\sqrt{K_m}} e^{-\delta_m r}. \quad (36)$$

We now return to our initial PE solution for a point source at 100 m. At 200 Hz, this waveguide contains 25 trapped modes. In Fig. 5(a), the standard pressure TL traces for a receiver at a depth of 30 m out to 4 km are presented. The solid curve displays the results from the MMPE model, while the dashed curve is based on solutions to Eq. (32) for the first 25 modes. The results agree quite well, with differences rarely exceeding 1 dB. The large difference observed at very short range (<200 m) is likely due to the source field approximation in the PE model, which only accounts for the surface-reflected image interference and neglects the bottom reflection at the source range. However, the MMPE model solutions are far-field solutions and should not be considered relevant at ranges less than a few water depths. Figures 5(b) and 5(c) show the corresponding comparisons for the radial and vertical components of the velocity TL trace computed from Eqs. (35) and (36), respectively. Again, the agreement is sufficient to confirm the implementation of the algorithm.

To confirm the normal mode expressions and ensure proper incorporation into the Couple97 model, the same range-independent scenario was used. Figure 6 displays the comparisons between the Couple97 model output and Eqs. (32), (35), and (36). For this calculation, only 25 modes were employed in Couple97. The solution was computed using the full, two-way coupled mode algorithm, although the solution with the one-way approximation was confirmed to be identical. While agreement is very good, we note that there are minor differences. This is presumably due to the higher accuracy of the Couple97 model, which accounts for complex eigenvalues and complex mode shapes when attenuation is present. The agreement between solutions for the particle velocity components is just as good as the pressure, suggesting that the calculations of velocity are being performed properly within the updated Couple97 model. We also note that direct comparisons between MMPE and Couple97 showed similar agreement.

Although the MMPE model is a well-tested, reasonably accurate model, it is not generally of benchmark quality. This is a known issue with PE models based on the split-step Fourier algorithm, primarily due to the treatment of the bottom interface which requires

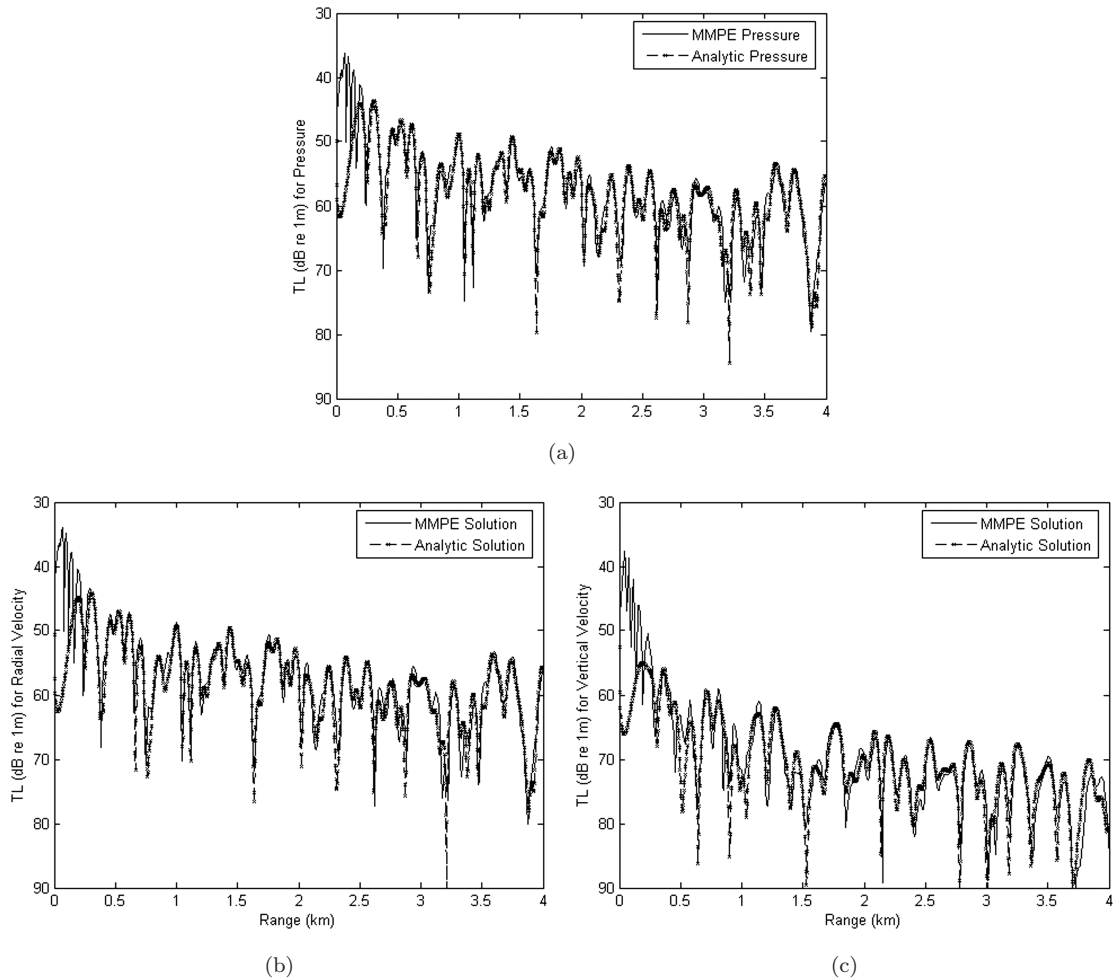


Fig. 5. Comparison of transmission loss traces at a depth of 30 m between MMPE solution (solid) and analytical solution (dash) for multiple mode calculation at 200 Hz: (a) pressure; (b) radial component of particle velocity; (c) vertical component of particle velocity.

the introduction of “mixing functions” to smooth the discontinuities over the computational mesh.^{7,10} One of the primary motivations of this analysis was the creation of a potential benchmark quality data set against which the MMPE results could be compared. Two-way, coupled mode models, such as Couple97, are capable of providing such accurate data sets.

Therefore, as a test of the model accuracy in a range-dependent environment, and to define a potential benchmark solution for other models, the standard ASA benchmark wedge with lossy bottom is employed. All the parameters chosen above for the lossy Pekeris waveguide correspond to the initial conditions of the benchmark wedge. We now make the bathymetry range-dependent by allowing the bottom interface to vary linearly with range from 200 m to 0 m over 4 km. In this case, the output of the two-way, coupled mode solution with 190 modes (the maximum the model will allow) will be used to validate the PE

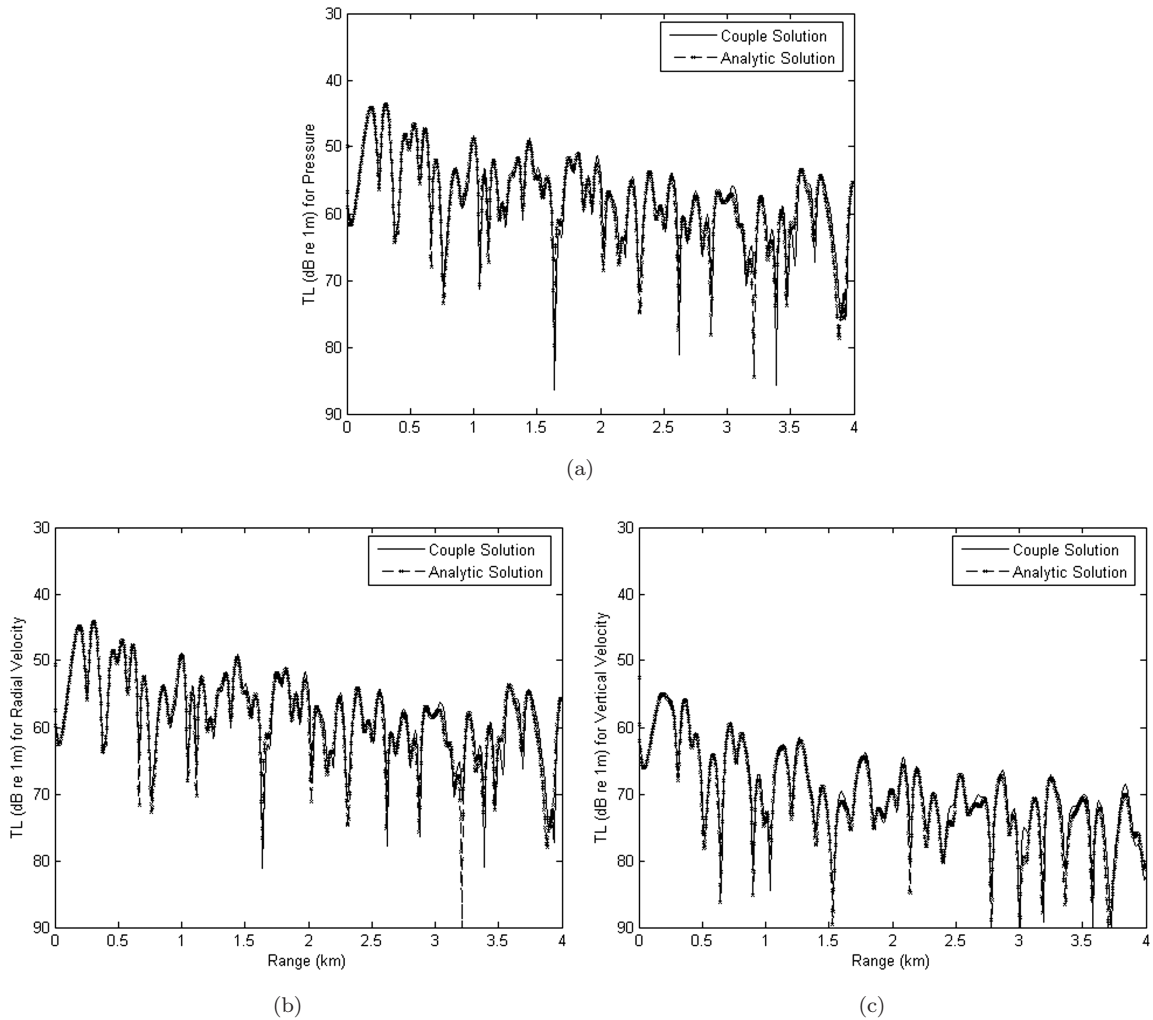


Fig. 6. Comparison of transmission loss traces at a depth of 30 m between Couple solution (solid) and analytical solution (dash) for multiple mode calculation: (a) pressure; (b) radial component of particle velocity; (c) vertical component of particle velocity.

results. Using this large number of modes should provide a reasonable approximation of the influence of the continuum on the solution. The model was run with the option of using an absorber at negative ranges, since fundamentally the model assumes that the environment is cylindrically symmetric. This has no impact on the solution at positive ranges away from the source.

Figure 7 displays the comparisons between the TL traces at 30 m depth for pressure, radial velocity, and vertical velocity. In each plot, the solid line corresponds to the results from the MMPE model, while the dashed line is the solution generated by the updated Couple97 model. As before, the comparisons are quite good, with generally less than a dB difference between the curves at most ranges of interest. The only exceptions are at

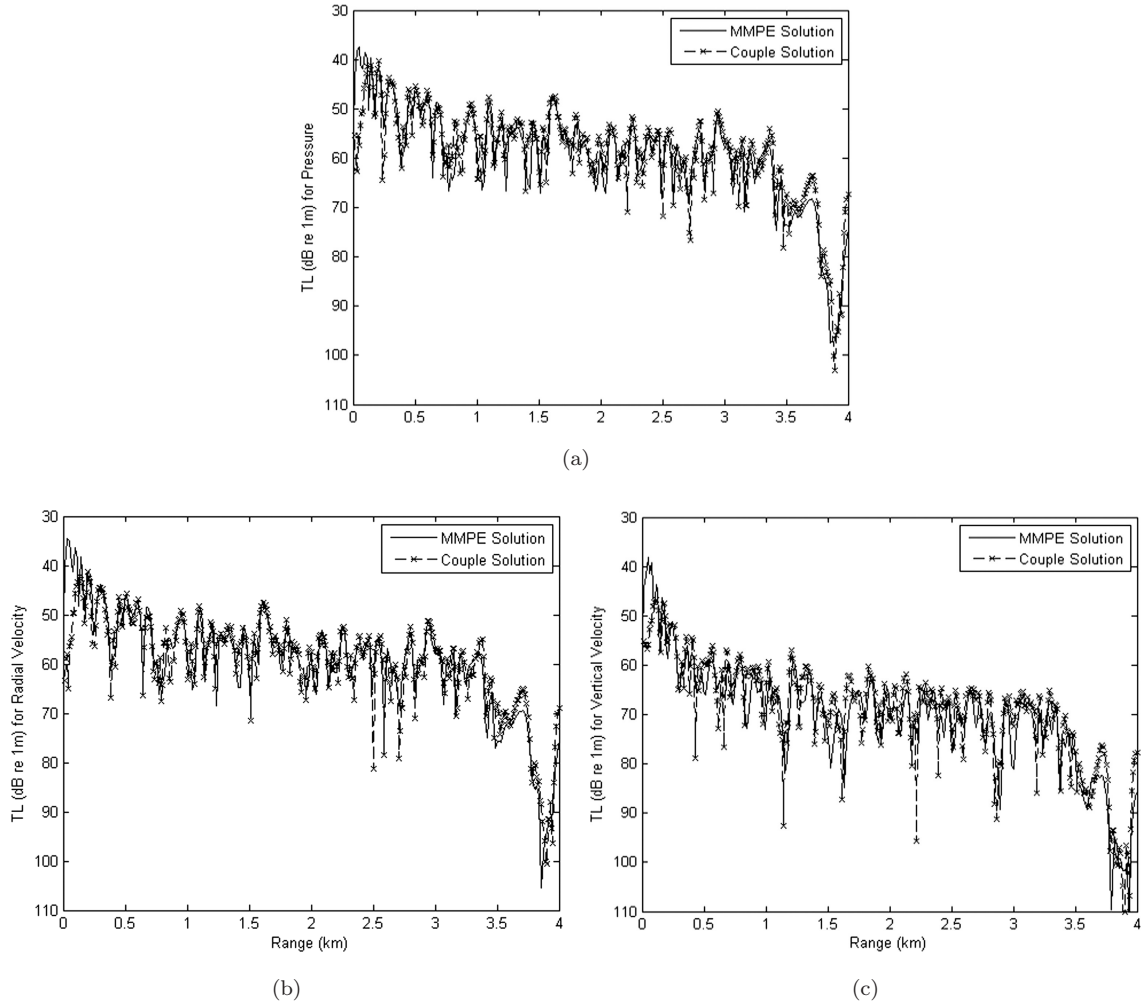


Fig. 7. Comparison of transmission loss traces at a depth of 30 m between MMPE solution (solid) and Couple solution (dash) for ASA benchmark wedge calculation at 200 Hz: (a) pressure; (b) radial component of particle velocity; (c) vertical component of particle velocity.

very short or very long ranges. At short range, as discussed previously, the MMPE source function overestimates the signal strength at high angles. At longer ranges, the MMPE solution appears to begin to degrade around 3.5 km. This corresponds roughly to the range at which the receiver trace depth is within the bottom medium. Additionally, the MMPE solution is known to degrade when the water depth is only a few wavelengths, again as a result of the bottom boundary condition. However, as the MMPE model is designed as a far-field model for predicting the acoustic field in shallow water, it performs well at those ranges where these conditions are satisfied. Accepting these limitations of the model, this analysis suggests that all expressions defined above are valid and the implementations are correct in both the PE and coupled mode models.

4. Summary

In this paper, numerical algorithms for calculations of the acoustic particle velocity field in general, range-dependent environments were presented for full-wave acoustic propagation models based on the parabolic equation and normal modes. The parabolic equation approach was straightforward, as it directly provides a means of evaluating the local, radial derivative of the pressure field. A similar approach would work with any parabolic equation propagation model. The accuracy of the vector field solution is then solely dependent upon the accuracy of the pressure field solution. The primary advantage of this approach is that it is based on the parabolic wave equation, and so can efficiently generate accurate solutions to the vector field in complex, range-dependent environments.

Expressions for computing the acoustic velocity components from normal mode models were also developed, including fully coupled, one-way coupled, and adiabatic propagation. Since the expressions were shown to be locally valid and independent of coupling between varying range segments, existing coupled mode codes utilized in benchmarking can be adapted to provide similar, benchmark-quality results for model assessment.

Several test cases were defined and employed to test the expressions and their implementations. A range-independent, Pekeris waveguide was employed with a single acoustic mode excited to examine the detailed structure of the velocity field and its associated angles of fluid motion. Approximate analytic solutions were used to compare the output of the PE model, which was found to produce the proper waveguide behavior. Similar analytic solutions for a point source in a lossy Pekeris waveguide were also used to compare *TL* calculations from the PE and coupled mode models. As before, the results agreed well with the predictions. Finally, the updated coupled mode model, Couple97, was used to generate potential benchmark data for the standard ASA lossy wedge, and the PE solutions were again found to be in good agreement.

While examining the CW fields in a simple, range-independent environment with significant multipath interference, multipath behavior of the particle motion was noted. Complex interference phenomena were found to produce variable angles of local energy flow. The interference was then examined in the context of normal modes, which also provided analytical functions for verification of the model results.

In future analysis with vector field modeling and/or processing, one should be careful to not consider the direction of the local acoustic flow as uniquely aligned with the direction of passing wavefronts. While this phenomenon may be well known to many researchers studying the vector field, it is not widely appreciated among many practitioners, in the opinion of the present author, and is worth reiterating. The interference of the wavefronts causes cyclic motion of the local medium and oscillatory fluctuations in the flow of energy. Just as this phase-coherent interference causes fluctuations in the amplitude of the pressure field, it also causes fluctuations in the direction of local energy flow. Thus, the local flow does not generally align with the passage of wavefronts we may associate with acoustic propagation through a region. Some spatial aperture, such as an array of sensors, is needed in order to unambiguously identify wavefront arrival angle information.

Acknowledgments

The author would like to express his deepest gratitude to Dr Richard Evans, the developer of the Couple97 model, for his guidance and feedback during the final edits of this paper. The author also wishes to thank the following persons for many useful discussions on particle velocity modeling and phenomena: Prof. Andres Laraaza (NPS), Dr Gerald D'Spain (MPL/SIO/UCSD), Prof. William Siegmann (RPI), Dr Roger Richards (NUWC-NPT), and Mr Phil Duckett (NUWC-NPT). The author is also grateful to the support provided by ONR Code 321OA, NUWC-NPT Code 15, and by the NPS sabbatical program.

References

1. J. A. Mann, J. Tichy and A. J. Romano, Instantaneous and time-averaged energy transfer in acoustic fields, *J. Acoust. Soc. Am.* **82** (1987) 17–29.
2. G. L. D'Spain, W. S. Hodgkiss and G. L. Edmonds, Energetics of the deep ocean's infrasonic sound field, *J. Acoust. Soc. Am.* **89** (1991) 1134–1158.
3. G. L. D'Spain, W. S. Hodgkiss and G. L. Edmonds, The simultaneous measurement of infrasonic acoustic particle velocity and acoustic pressure in the ocean by freely drifting Swallow floats, *IEEE J. Oceanic Eng.* **16** (1991) 195–207.
4. A. Nehorai, Acoustic vector-sensor array processing, *IEEE Trans. Sig. Proc.* **42** (1994) 2481–2491.
5. M. Hawkes and A. Nehorai, Acoustic vector-sensor beamforming and capon direction estimation, *IEEE Trans. Sig. Proc.* **46** (1998) 2291–2304.
6. B. A. Cray and A. H. Nuttall, Directivity factors for linear arrays of velocity sensors, *J. Acoust. Soc. Am.* **110** (2001) 324–331.
7. K. B. Smith and F. D. Tappert, UMPE: The University of Miami parabolic equation model, Version 1.0, Marine Physical Laboratory Technical Memo (1993), p. 432.
8. K. B. Smith, G. L. D'Spain and W. S. Hodgkiss, Modeling acoustic particle velocity in range dependent environments with a parabolic equation code, *J. Acoust. Soc. Am.* **94** (1993) 1885.
9. R. H. Hardin and F. D. Tappert, Applications of the split-step Fourier method to the numerical solution of nonlinear and variable coefficient wave equations, *SIAM Rev.* **15** (1973) 423.
10. K. B. Smith, Convergence, stability and variability of shallow water acoustic predictions using a split-step Fourier parabolic equation model, *J. Comp. Acoust.* **9** (2001) 243–285.
11. D. J. Thomson and N. R. Chapman, A wide-angle split-step algorithm for the parabolic equation, *J. Acoust. Soc. Am.* **74** (1983) 1848–1854.
12. F. B. Jensen, W. A. Kuperman, M. B. Porter and H. Schmidt, *Computational Ocean Acoustics* (AIP, New York, 1994), pp. 257–323.
13. R. B. Evans, A coupled mode solution for acoustic propagation in a waveguide with stepwise depth variations of a penetrable bottom, *J. Acoust. Soc. Am.* **74** (1983) 188–195.
14. F. B. Jensen and C. M. Ferla, Numerical solutions of range-dependent benchmark problems in ocean acoustics, *J. Acoust. Soc. Am.* **87** (1990) 1499–1510.

Copyright of Journal of Computational Acoustics is the property of World Scientific Publishing Company and its content may not be copied or emailed to multiple sites or posted to a listserv without the copyright holder's express written permission. However, users may print, download, or email articles for individual use.